ARTICLE

On the origin of non-monotonic variation of lattice parameters of $LiNi_{1/3}Co_{1/3}Mn_{1/3}O_2$ with lithiation/delithiation: a first-principles study†

Received 00th January 20xx,
Accepted 00th January 20xx

DOI: 10.1039/x0xx00000x

Liang-Yin Kuo, [a,b] Olivier Guillon [b] and Payam Kaghazchi *[b]

Here, we show that the non-monotonic variation of lattice parameters of $Li_xNi_{1/3}Co_{1/3}Mn_{1/3}O_2$ during delithiation/lithiation can be predicted in good agreement with experimental results by applying an approach combining an extensive set of Coulomb energy and density functional theory calculations. Moreover, the influence of choosing exchange-correlation functional on our results is discussed. By analyzing local spin polarization, spin density plot, density of states, and Bader charges, the reason behind this behavior is explained. It is found that the presence/absence of electrostatic Li–O interactions and Jahn–Teller distortion as well as oxidation of O anions are key parameters to control the lattice parameter changes. In particular, the contraction of c for $0.5 > x$, which has not been fully explained so far, is found to be due to the vanishing of Jahn–Teller distortion of NiO_6 octahedra. The O3 → O1 phase transition for low concentrations of Li, which also has not been justified until now, is shown to be driven by strongthening of ionic bonds and electrostatic interaction in the latter phase.

Introduction

Although $LiCoO_2$ (LCO) is the most widely used cathode material for lithium-ion batteries (LIBs) in small-scale devices,[1,2] it is not a suitable candidate for LIBs in electric vehicles because of its low energy density and the high cost of Co metal.[3] The major reason for the low energy density is its structural instability (due to a large volume change and/or phase transition) upon more than half delithiation. Thus, the charging process should be restricted under this level resulting in a low practical voltage of LCO.[4] $LiNiO_2$ (LNO) has the same space group and atomic structure as LCO, while it consists of low-cost Ni metal and provides higher energy density than LCO as more Li ions can be safely (from the structural stability point of view) extracted from LNO during charging. The structural instability occurs only after removing ~0.75 Li content.[5] However, thermal instability (due to the high reactivity with electrolyte) of LNO is more severe than in LCO.[6,7] $LiMnO_2$ (LMO) contains Mn which is cheaper and less toxic than Co and Ni metals.[8] Moreover, it provides higher safety (thermal stability) than LCO and LNO. However, LMO possesses a lower energy density (due to a lower structural stability) than LCO and LNO.[9,10] To combine advantages of LCO, LNO, and LMO, $LiNi_xCo_yMn_{1-x-y}O_2$ cathodes were proposed, synthesized, and even commercialized.[11] Among various possible NCM systems with different Ni, Co, and Mn ratios, $LiNi_{1/3}Co_{1/3}Mn_{1/3}O_2$ (hereafter called NCM111) is one of the most commonly-used and -studied system.[12–14] The structural stability of NCM111 is higher than LCO, as the cracking of NCM111 microstructures that leads to their voltage and capacity fade[15–22] occurs at higher levels of lithiation/delithiation in comparison to LCO. The main reason behind the microstructure cracking of cathode materials such as NCM111 is an anisotropic change in their lattice parameters during charge/discharge. Understanding mechanism of this phenomenon is therefore important to improve the performance of NCM cathode materials.

During charging (i.e. delithiation), the lattice parameter a (a = b) of $Li_xNi_{1/3}Co_{1/3}Mn_{1/3}O_2$ (hereafter called LixNCM111) contracts for $1.00 > x > 0.35$, while it expands for $0.35 > x$.[23] However, the lattice parameter *c* expands for $1.00 > x > 0.51$ and then it contracts for $0.51 > x > 0.29$.24 These changes in a and *c* cause the unit cell volume to contract slightly for $1.00 > x > 0.35$ and then strongly for $0.35 > x$.[23] Experimental measurements by Li *et al.*[25] showed that the contraction of *a* is because of the delithiation-induced oxidation of transition metal (TM) cations that reduce their ionic radii. The expansion of *c* in NCM111 was mainly explained to be because of increase in the electrostatic O–O repulsive force resulting from the weakening of screening of O charge by Li ions during delithiation.[26,27] However, the contraction of c-axis in NCM cathodes for $x < 0.50$ has not been fully explained. The most common belief is that oxidation of O anions (together with TM cations) at high delithiation levels weakens interlayer O–O repulsions leading to the contraction of *c*.[16] The delithiation-induced decrease in negative charge of O[28] and/or stronger TM–O bonds (due to more hybridization of TM–O orbitals)[29] had been proposed before by theoreticians.

Density functional theory (DFT) has been applied to simulate lattice parameters (i.e. unit cell volume) change through delithiation.

[a] Physikalische und Theoretische Chemie, Freie Universität Berlin, Arnimallee 22, D-14195 Berlin, Germany. E-Mail: kuoliangyin@zedat.fu-berlin.de
[b] Forschungszentrum Jülich GmbH, Institute of Energy and Climate Research, Materials Synthesis and Processing (IEK-1), D-52425, Jülich, Germany. E-Mail: o.guillon@fz-juelich.de; p.kaghazchi@fz-juelich.de

†Electronic Supplementary Information (ESI) available: See DOI: 10.1039/x0xx00000x

For example, DFT calculation (using the local density approximation LDA functional) by Koyama *et al.*[30] found that the parameter a decreases from x = 1.00 to x = 0.33, while it increases from x = 0.33 to x = 0.00. However, it is known that NCM111 undergoes a phase transition from O3 to O1 for very deep delithiation levels, i.e. x < 0.23.[23] Moreover, they found that the c value increases monotonically from x = 1.00 to x = 0.33, while it decreases from x = 0.33 to x = 0.00.[30] However, experimental results show that the contraction of c starts for x < 0.51. Hwang *et al.*[29] used the more accurate generalized gradient approximation (GGA) of Perdew-Burke-Ernzerhof (PBE)[31] functional compared to LDA for their DFT calculation to study this system. They found that the size of a decreases from x = 1.00 to x = 0.50, while it increases from x = 0.50 to x = 0.00. However, according to the experimental data, increase in a should occur after removing 0.67 Li.[23] Furthermore, their results show that the c value increases from x = 1.00 to x = 0.33 and decreases from x = 0.33 to x = 0.00. The decrease in the c value from x = 0.33 to x = 0.17 was calculated to be only 0.018 Å. In addition, they found that the value of c for x = 0.17 is 0.71 Å higher than the value of c for x = 1.00. Experimental measurements, however, reported that the c value for x < 0.30 is 0.39 Å shorter than that for x = 1.00.[26] Min *et al.*[32] carried out GGA-PBE calculation to study NCM with different Ni contents. They showed that the value of a decreases from x = 1.00 to x ≈ 0.35 and then increases from x ≈ 0.35 to x = 0.00 state. However, the c value increases from x = 1.00 to x ≈ 0.35 and then decreases for x ≈ 0.35 to x = 0.00. They proposed that the experimental results can be reproduced only by considering a layer-by-layer delithiation mechanism, which has not been reported so far by any experimental or other theoretical studies. A comparison between the aforementioned theoretical studies shows that the model structure (arrangement of TMs and Li ions), type of exchange-correlation (XC) functional, and computational setup (e.g. spin polarization) are key points in modelling and understanding lattice parameter changes with delithiation. In these studies, in order to find the arrangement of Li ions for various Li concentrations, a series of DFT calculations[29,30] or cluster expansion (CE) has been applied.[32] Both cases have advantages and disadvantages. Sampling of configurations by DFT calculation is limited by the computational cost and time. Applying the CE method can misguide us to find minimum-energy structures for systems where magnetization of TM cations is very sensitive to the concentration and arrangement of Li ions. The other more promising types of XC functionals for studying metal-oxide systems such as PBE+U[33] has been studied for Ni-rich NCM[50], while Heyd-Scuseria-Ernzerhof (HSE)[34] as well as the recently-developed SCAN (Strongly Constrained and Appropriately Normed)[35–38] functional have not been so far applied to study lattice change in NCMxy1-x-y cathodes. Recently, Chakraborty *et al.*[39] have calculated lattice parameters, magnetic moments, density of states, and voltage profiles of LCO, LNO, and LMO at different lithiated/delithiated states by using the DFT-PBE, PBE+U, and SCAN. Their results showed that the SCAN functional performs better than the PBE functional for the prediction of band-gaps, while better than PBE+U functional for DOS, and better than both PBE and PBE+U functionals for lattice parameters.[36]

In this work, by combining an extensive Coulomb energy analysis and DFT calculations, we obtained the Li arrangement in LixNCM111 as a function of Li concentration x. The influence of exchange-correlation functional, in particular SCAN, on the calculated lattice parameters is discussed. By analyzing electronic and atomic structures, the reason of non-monotonic change of lattice dimensions in NCM111 will be explained.

Results and discussion

Our DFT-PBE calculations, in agreement with a previous DFT-HSE06 study,[44] showed that a homogenous distribution of TM cations in the fully-lithiated NCM111 (Li1.00NCM111) is the most favourable structure (see Fig. S1 in SI). Focusing on this structure, we explored the most favourable arrangement of Li ions in Li sites for various Li concentrations x in LixNCM111. To achieve this aim, we first calculated total Coulomb energies (E_C) of a large number of possible configurations for each Li concentration as follows. For Li0.67NCM111 and Li0.33NCM111, which were modelled with 1×1×1 unit cells (only for Coulomb energy analysis), we considered all possible arrangements of Li ions in Li sites, namely $\frac{9!}{6!3!} = 84$ configurations. However, for Li0.50NCM111, which we had to model it with a 2×2×1 supercell, there exists a large number of possible configurations of $\frac{36!}{18!18!} = 9.075 \cdot 10^9$, which is computationally intractable. In this case, the most favorable structure of Li0.67NCM111 with a 2×2×1 supercell was considered and all possible arrangements of 18 Li ions in 24 occupied Li sites, namely $\frac{24!}{6!18!} = 134596$ configurations were modelled. For Li0.17NCM111, we considered all possible Li arrangements in Li sites in a 2×2×1 supercell and modelled $\frac{36!}{30!6!} = 1947792$ structures. Two sets of charge values, i.e. two charge-balancing mechanisms, were considered for computing total Coulomb energies. I) elementary charge values of 3.00+, 3.33+, 3.50+, 3.67+, and 3.83+ for each TM (Ni, Co and Mn) cations at x = 1.00, x = 0.67, x = 0.50, x = 0.33, and x = 0.17, respectively and II) charge values of 2+, 3+, 4+ for Ni, 3+ and 4+ for Co depending on the Li concentration, and 4+ for Mn. For both mechanisms we considered elementary charges of 1+ for Li and 2− for O, respectively.

Calculated E_C values for configurations 1-50 with charge balancing mechanism I and II are illustrated in Fig. 1. For Li0.67NCM111 and Li0.33NCM111, we performed DFT-PBE calculation for 6 and 10 distinguishable structures with lowest E_c values. The DFT-PBE-calculated most favourable structures for x = 0.67 (configuration vi) and x = 0.33 (configuration i) possess well-ordered hexagonal arrangements of Li ions at each layer. Since the lowest (DFT-PBE) total-energy structure was among the low-energy Coulomb energy analysis with mechanism I for Li0.33NCM111 and Li0.67NCM111, we further considered only mechanism I to determine the electrostatically most favorable structures for Li0.50NCM111. Afterward, we performed DFT-PBE calculations for 7 distinguishable Li arrangements with the lowest E_c values. The configuration v was

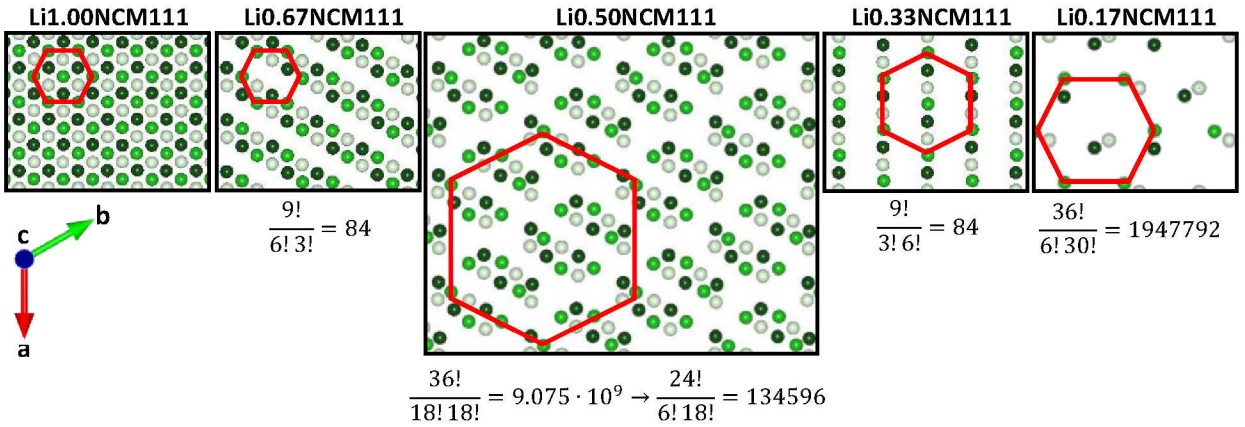

Fig. 1 Top views of Li layers in the most favourable structures as well as considered number of configurations for the Coulomb-energy analysis for LixNCM111 with various Li concentrations *x*.

then found to be the minimum-total-energy structure. Furthermore, 3 well-ordered arrangements of Li ions (Fig. S3: viii, ix, x) were modelled from the configuration v. These 3 configurations were investigated because for Li0.50NCM111 we had to start with the structure of Li0.67NCM111 and, therefore, we might have missed some important (symmetric) structures. Comparing total energies of all 10 (7+3) DFT-PBE calculations showed that the most favourable structure is configuration x. Finally, for Li0.17NCM111, we carried out 50 DFT-PBE calculations for topmost favourable structures determined after performing 1947792 total Coulomb-energy calculations. The minimum total-energy structure according to DFT-PBE, namely configuration v, was found to have a well-ordered hexagonal arrangement of Li ions at each layer (see Fig. S3 in SI).

The computed lattice parameters ($a = b$ and c) and corresponding volume changes for LixNCM111 using DFT-PBE, PBE+*U*, and SCAN are illustrated in Fig. 2. All three XC functionals indicate that the value of a decreases with delithiation from $x = 1.00$ to $x = 0.33$ and increases from $x = 0.33$ to $x = 0.17$. However, the value of c expands from $x = 1.00$ to $x = 0.50$, and then it shrinks slightly for $x = 0.50 \rightarrow 0.33$, and finally it decreases significantly for $x = 0.33 \rightarrow 0.17$. The maximum value of c is found for $x = 0.50$. Nevertheless, the volume always decreases from $x = 1.00$ to $x = 0.17$, being more significant for $x = 0.33$ to $x = 0.17$. Although the DFT-PBE and SCAN results are similar, but, generally, calculated absolute values and changes in a, c, and volume with the latter functional is more comparable to the experimental data. For example, the volume decrease ΔV for $x = 1.00 \rightarrow x = 0.33$ is −1.83 % and −3.32 %, respectively, with DFT-PBE and SCAN functionals. The latter functional predicts that (using a linear interpolation) $c = 13.877$ Å, $a = 2.841$ Å, and $\Delta V = -4.61\%$ for $x = 0.30$. In comparison to DFT-PBE and PBE+*U* results, the DFT-SCAN data are closer to the experimental values of $c = 13.876(1)$ Å, $a = 2.829(1)$ Å, and $\Delta V = -5.14\%$ (see Fig. 2) by Hua *et al.*[26] reported for LixNCM111 with $x < \sim 0.30$ Li. The variation of a and volume with x is found to be larger with DFT-PBE+*U* than the other two functionals as well as the experimental data by Petersburg *et al.*[24] and Hua *et al.*[26] The DFT-PBE+*U*-overestimated decrease in volume is because of overestimation of decrease in a value. Comparing calculated a, c, and volume with various *U* values for Ni (see Fig. S2 in SI), we find no significant changes for $0.33 < x < 1.00$, where only oxidation of Ni cations occur as will be discuss later in this article. However, for $x < 0.33$, where oxidation of Co cations occurs, the important role of charge localization on Ni cations to determine the lattice sizes appears. As it will be discussed later, the increase in the value of a for $x < 0.33$ is due to the strengthening of electrostatic repulsion between TM cations. Non-realistic delocalization of holes on Ni cations which arises by considering smaller *U* values cannot reproduce the experimental data showing the increase of a parameter.

To find the reason behind lattice parameters and volume change, we further calculated local number of unpaired spin $N^{\uparrow}-N^{\downarrow}$ (NUS), spin density difference (SDD), and density of states (DOS) illustrated in Fig. 3 as well as Bader charges and bond lengths shown in Fig. 4. Our results show that SCAN predicts more reasonable NUS values than the other two functionals. For example, calculated total NUS values of 58.5, 46.5, and 35.6 with SCAN for Li1.00NCM111, Li0.67NCM111, and Li0.33NCM111, respectively, are in good agreement with the NUS values of 60 (NUS for Ni: 12×2 and NUS for Mn: 12×3), 48 (NUS for Ni: 12×1 and NUS for Mn: 12×3), and 36 (NUS for Mn: 12×3) which are expected for $Li_xNi_{12}Co_{12}Mn_{12}O_{72}$ supercells with pure ionic bonds when considering formal charge states of ions. Calculated NUS values with different XC functionals as well as those which are expected for pure ionic crystals of LixNCM111 are listed in Table S1 of SI. In addition, as mentioned before, calculated lattice parameters with SCAN are more comparable to measurements. We therefore continued our analayzis by using DFT-SCAN calculation. We focused on the following Li concentrations: $x = 1.00$, 0.67, and 0.33, since a similar electronic configuration is expected for each type of TM cations. It is worth mentioning that the DOS of *d* orbitals of Ni, Co, and Mn is clearly different (see Fig. 3) from that of a simple t_{2g}-e_g splitting model. For example, from the classical picture, the electronic configuration of Ni cations is expected to be $t_{2g}^6e_g^2$. However, besides occupations of up-spin and down-spin of t_{2g} and up-spin of e_g orbitals for Ni cations, a partial occupation of down-spin

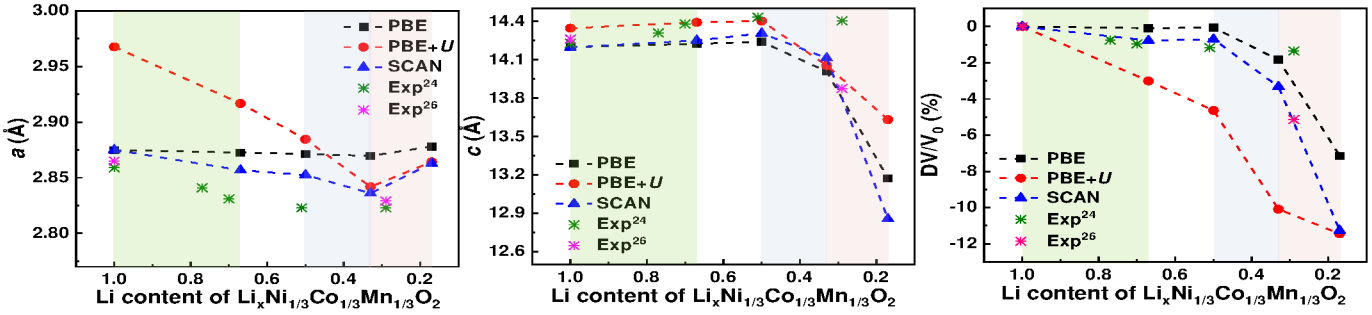

Fig. 2 Calculated variation of lattice parameters and unit cell volume of LixNCM111 with delithiation using DFT-PBE, PBE+*U* (U_{Ni} = 6.8 eV, U_{Co} = 5.9 eV, and U_{Mn} = 5.2 eV), and SCAN functional. Experimental results are also given for comparison.

of e_g and a depletion of down-spin of t_{2g} is also observed in the DOS plot. This is because of a large overlap between t_{2g} and e_g orbitals for all TM cations at all Li concentrations. The overlap and broadening of t_{2g} and e_g orbitals lead to uncertainty in determining electronic configuration of TM cations. Thus, as will be shown in the following a detailed analysis of NUS, SDD, and Bader charge together with DOS is indispensable.

Li1.00NCM111 The SDD plot shows unpaired up-spin on all O anions indicating that O atoms are not completely reduced. The SDD feature on Mn is larger than that on Ni confirming that the oxidation state on the former is larger. However, in both cases, the charge state is lower than that expected: 1.64+ for Ni and 3.87+ for Mn. For sake of simplicity, in the following, we discuss our SDD results with respect to a complete ionic system. The up-spin electrons (yellow isosurface) on *p*(O) are directed toward Ni confirming back donation of down-spin electrons to e_g(Ni) orbitals. The existence of down-spin states at −0.80 eV ≤ $\varepsilon - \varepsilon_F$ ≤ −0.15 eV in DOS of e_g(Ni), i.e. d_{z^2}(Ni) and $d_{x^2-y^2}$ (Ni), confirms this hypothesis. The non-zero NUS (0.03) together with DOS peaks in −0.86 eV ≤ $\varepsilon - \varepsilon_F$ ≤ 0.20 eV for Co cations show partial up-spin and down-spin occupation of e_g states, the latter being slightly larger in particular for $d_{x^2-y^2}$(Co). These results indicate that Co cations have charge states slightly lower than 3+ charge. The SDD on Co cations, however, is so small that is not observed with a 0.004 isosurface. The down-spin electrons (blue isosurface) on *p*(O) orbitals towards *d*(Mn) orbitals are arising from an up-spin electron transfer from *p*(O) to e_g(Mn). The corresponding DOS plot shows the presence of e_g(Mn) features (more up-spin states) in −1.58 eV ≤ $\varepsilon - \varepsilon_F$ ≤ −0.18 eV. Moreover, a back-donation of down-spin electrons from *p*(O) to t_{2g}(Mn) with pre-existing three up-spin electrons can also be observed in −7.10 eV ≤ $\varepsilon - \varepsilon_F$ ≤ −4.91 eV. Back donation of electrons from O to TMs can be indication of existence of partial covalent bonding between TM and O in the full lithiated NCM111. It is hard to conclude such bonding from our DOS data. TM–O covalency has also been reported for fully lithiated LMO by experimentalists[49] and fully lithiated NCM811 by theoreticians.[50] From the DOS data, we find a band gap of 0.56 eV confirming the semiconductor nature of Li1.00NCM111. The DOS plots also demonstrate that the e_g states of Ni as well as the t_{2g} states of Co are close to the Fermi level and are likely to be depleted with delithiation. The Bader charge analysis (Fig. 4a) will be discussed for the lower lithium concentration cases since only the relative values can help us to analyse oxidation or reduction of ions.

Li0.67NCM111 Oxidation of Ni cations with respect to the full lithiation state can be recognized by comparing the DOS plots for Li1.00NCM111 and Li0.67NCM11 where up-spin features close to ε_F, i.e. e_g(Ni) states, become narrower and lower in the latter case. The SDD plots also show oxidation of all Ni cations as their SDDs become smaller after extracting 0.33 Li. This can also be qualitatively concluded from the Bader charge analysis where an oxidation of 0.14 $|e|$ observed. Since the up-spin d_{z^2}(Ni) states are larger than the $d_{x^2-y^2}$(Ni) ones at −0.61 eV ≤ $\varepsilon - \varepsilon_F$ ≤ −0.19 eV, and the SDD features are d_{z^2} like we propose that the electron is removed from $d_{x^2-y^2}$ (Ni) orbital. The delithiation-induced electron removal from $d_{x^2-y^2}$ orbital of Ni^{2+} has also been proposed by Radin *et al.*[51] for Ni-based cathodes. A similar oxidation mechanism has also been reported by Dompablo *et al.*[52] based on DFT-PBE calculated Ni–O bond lengths. From the averaged NUS value of 0.80 for Ni we estimated the charge state of Ni to be 2.48+ for *x* = 0.67 as Ni is oxidized by 0.84 $|e|$. Hoang *et al.* have calculated NUS for Ni^{2+} to be 0.91.[44] One important result of formation of $Ni^{(3-\Delta)+}$ is the creation of Jahn-Teller (J–T) distortion upon which the average axial Ni–O bond lengths ($\bar{d}^{Ni}_{axial}$ = 2.04 Å) are longer than the average equatorial Ni–O bond lengths ($\bar{d}^{Ni}_{equatorial}$ = 1.93 Å). A similar result to our calculation has been reported by Hoang *et al.* using DFT-HSE calculation: two long Ni–O bonds of 2.07 Å and four short Ni–O bonds of 1.91 Å.[44] The J–T effect for Ni^{3+} has also been observed by experimental measurements.[24,55] The corresponding SDD plot clearly shows an enlargement of up-spin electrons on *p* orbitals of each O anion overlapping with d_{z^2} orbitals of Ni cations, hereafter called *p*(O2). This accompanies with the contraction of axial O2–Ni–O2 bond lengths. Small parts of the topmost e_g states of Co and Mn disappear as well. This means that Co and Mn are also partially oxidized. The Bader charge values, also, confirm that, in comparison to *x* = 1.00, Co and Mn are slightly oxidized. The oxidation state of Co cannot be estimated from the change in NUS value. This is because there are both up-spin and down-spin electron transfers from Co to O. Thus, the local NUS value on Co changes slightly from −0.03 (*x* = 1.00) to −0.02 (*x* = 0.67). In this case, the Bader charge values help to conclude that oxidation of Co (0.024 $|e|$) is higher than that of Mn (0.008 $|e|$). A comparison between SDD for *x* = 1.00 and *x* = 0.67

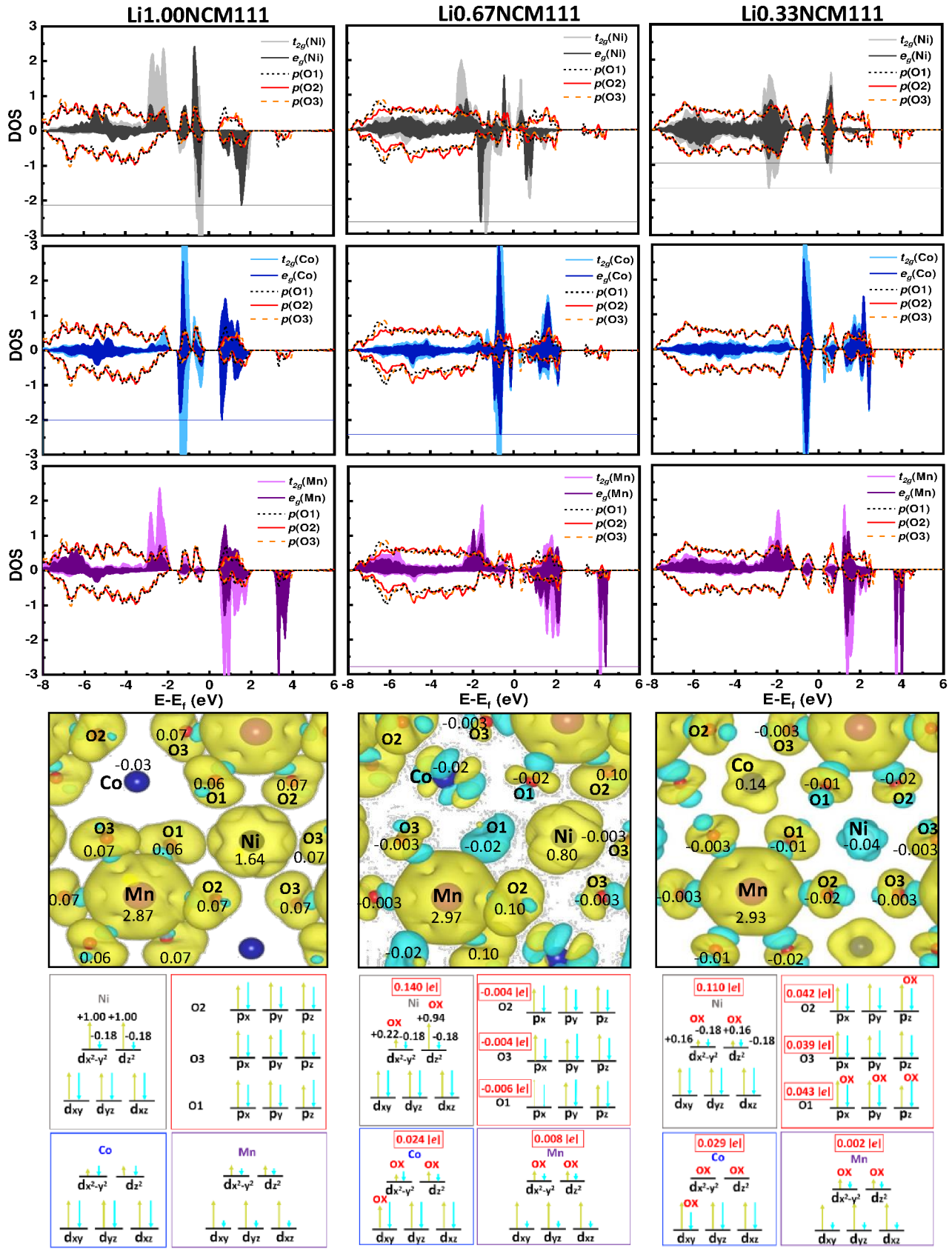

Fig. 3 Density of states (DOS), spatial spin density difference (SDD) with average local numbers of unpaired spin (NUS) on each ion, and proposed electronic configurations with average Bader charges (in |e|) in the most favorable LixNCM111 structures based on DFT-SCAN calculation. Ni, Co, Mn, and O are in gray, blue, purple, and red, respectively. The atomic coordinates were rotated about the b_y-axis to align axial TM–O bonds (in TMO_6 octahedra) along the global c_z-axis of the unit cell to assign the e_g and representative t_{2g} states. Up-and down-spins in SDD are in yellow and blue, respectively.

confirms a slight internal down-spin electron transfer from e_g(Co) to p(O3) and probably a slight delithiation-induced oxidation. The DOS plots show a large overlap between e_g(Ni) and e_g(Co) with p(O) at -0.27 eV ≤ $\varepsilon - \varepsilon_F \leq -0.01$ eV, but a very small overlap between e_g(Mn) and p(O). This indicates that the internal electron transfers are mainly between Ni and Co with O. Considering changes in SDD and Bader charge variation (−0.005 $|e|$) on O anions (see the last sentences of this paragraph) as well as increase of NUS by 0.10 and Bader charge by 0.008 $|e|$ on Mn for x = 1.00 → x = 0.67, we conclude a partial down-spin electron transfer from d(Mn), probably from e_g, to p(O1) and p(O3). Moreover, there should be a delithiation-induced oxidation of Mn since the amount of O reduction is much smaller than the oxidation of Mn. Note that the oxidation of Mn cannot be observed by comparing the SDD plots for x = 1.00 and x = 0.67 cases since the spin density variation is considerably smaller than the original spin density of Mn cations. No clear J–T distortion is observed for $Co^{(3-\Delta)+}$ and $Mn^{(4-\Delta)+}$, which is in line with previous experimental[24] and theoretical[20] studies.

The small difference between $\bar{d}^{Co}_{axial} = 3.90$ Å and $\bar{d}^{Co}_{equatorial} = 3.87$ Å as well as $\bar{d}^{Mn}_{axial} = 3.88$ Å and $\bar{d}^{Mn}_{equatorial} = 3.79$ Å in Co–O and Mn–O octahedra, respectively, is induced due to J–T distortion in Ni–O and symmetry breaking due to the partial oxidation of Co and Mn. The Bader charge analysis indicates that in average all three types of O anions are slightly reduced when x = 1.00 → x = 0.67. The local NUS and SDD of O and TM cations help us to find the mechanism of O anions reduction, which is governed by the transfer of up- and down-spin electrons from TMs to Os. The SDD figures indicate an up-spin electron transfer from e_g(Ni) to p(O2), while down-spin from e_g(Co) and e_g(Mn) to p(O3) and p(O1). Appearance of up-spin (yellow-colour) on Co is indication of down-spin electrons from Co to O. However, the overall reduction of O anions is very small, which might be indication of partial oxidation of O anions, besides the electron transfers from TMs to Os. Oxidation of O has been also reported by experiment[59] and theory[28,50]. Similar to the case of Li1.00NCM111, we cannot comment on the formation of TM–O covalent bonds from our DOS data, but partial electron pairing in TMs orbitals might be indication of such bonds in Li0.67NCM111.

Li0.33NCM111 Upon delithiation (x = 0.67 → x = 0.33) the topmost features of d orbitals of Ni below ε_F (down to around −2 eV), namely shallow dz^2(Ni) states, disappear indicating a further oxidation of Ni ions. The SDD plots clearly show the oxidation of Ni cations as well. The Bader charge analysis also qualitatively confirms the oxidation of Ni (by 0.11 $|e|$). The delithiation-induced oxidation of dz^2(Ni) for x = 0.67 → x = 0.33 agrees with previous experimental[56] and theoretical[29] studies. From the average NUS value of −0.04 on Ni, we estimate a removal of 0.84 up-spin electrons from e_g(Ni) and a charge state of 3.32+ at x = 0.33. Calculated average NUS values of −0.11[60], 0.00[61], and 0.10[50] (absolute NUS) have been reported for Ni^{4+} in NCM systems by performing DFT-PBE+U and DFT-PBE calculation. The coexistence of both spin states in e_g(Ni) can be seen from the DOS plot showing down-spin and up-spin features at -0.87 eV ≤ $\varepsilon - \varepsilon_F \leq -0.17$ eV, the downward peaks being larger. An overlap between e_g(Ni) and p(O) at the aforementioned energy range indicates that a small up-spin electron transfer from Ni to O is possible. The formation of $Ni^{(4-\Delta)+}$ leads to the suppression of Jahn-Teller (J–T) distortion where $\bar{d}^{Ni}_{axial} = 3.79$ Å becomes comparable to $\bar{d}^{Ni}_{equatorial} = 3.78$ Å. The absence of J–T distortion in Ni^{4+}–O has also been reported in previous experimental[24] and theoretical[30] works. A comparison between NUS values for x = 0.67 and x = 0.33 does not provide a certain quantitative value for oxidation of Co. Nevertheless, the Bader charge analysis shows a larger oxidation of Co compared to Mn. Experimental study by Saadoune *et al.*[62] has also proposed that the oxidation of Co cations starts before all Ni cations are completely oxidized. The disappearance of down-spin states in the DOS plot of Co at -0.32 eV ≤ $\varepsilon - \varepsilon_F \leq -0.02$ eV when x = 0.67 → x = 0.33 as well as a slightly larger density of up-spin states in the DOS plot of the latter case indicates that the yellow-colour of SDD on Co is due to the removal of down-spin electron from Co. An electron transfer from O to Co is not observed in the DOS plots as no p(O) state exist below ε_F. The NUS data shows a back-donation of 0.04 down-spin electrons from O anions to e_g(Mn), showing the reduction of Mn by ∼0.04 $|e|$. The electron transfer can be confirmed from an overlap between e_g(Mn) and p(O) states in the energy range of -0.87 eV ≤ $\varepsilon - \varepsilon_F \leq -0.17$ eV which can be seen in the corresponding DOS plot. An averaged value of 0.12 up-spin electron is removed from p(O1) anions. Moreover, there is a very small down-spin electron oxidation and/or transfer (to Mn) from p(O3) and p(O1) anions meaning a small oxidation of these O anions compared to x = 0.67. The average oxidation of all O anions is estimated to be 0.037 $|e|$ which is 0.008 $|e|$ larger than that of Co cations. Note that the majority of electron removal occurs from O1. Comparing DOSs shows a clear hybridization between d(Ni) and p(O) orbitals for -7.84 eV ≤ $\varepsilon - \varepsilon_F \leq -1.09$ eV in Li0.33NCM111 which is not observed in Li1.00NCM111 and Li0.67NCM111. This result is in line with previous experimental[25] and theoretical[29] studies reporting a stronger Ni–O covalency at low Li contents.

Bader charge and TM–O bond length results in Fig. 4 indicate oxidation of several $Ni^{(3-\Delta)+}$ cations and suppression of J–T distortion in their NiO_6 octahedra when 0.17 Li is removed from Li0.67NCM111. The O anions are slightly oxidized when x = 0.67 → 0.50. Figure 4 shows that a strong oxidation of O anions occurs for x = 0.33 → 0.17, similar to the case of x = 0.50 → 0.33. We also find that some of Co anions start to oxidize strongly when x = 0.33 → 0.17 (see Fig. S4 in SI).

Fig. 4b shows the average projected O–O separation on the c axis for the O–TM–O intralayer (d_1) and that for the O–TM–O interlayer (d_2). Removing 0.33 Li from Li1.00NCM111 causes d_1 to shrink by 2.15 %, which is due to the radius contraction of all Ni cations that are oxidized (see the SDD plots and NUS values in Fig. 3 as well as Bader charge analysis in Fig. 4a) in Li0.67NCM111 with respect to Li1.00NCM111. Due to the J–T distortion for $Ni^{(3-\Delta)+}$, axial Ni–O bond lengths only slightly shrink (by 0.02 Å), while equatorial Ni–O bond lengths contract by 0.2 Å in the delithiated case compared to the full-lithiated one. However, d_2 expands by 2.40 % when x = 1.00 → 0.67. According to a previous explanation,[26] this is due to the weakening of screening of O charges by Li ions. Our Bader charge calculations in

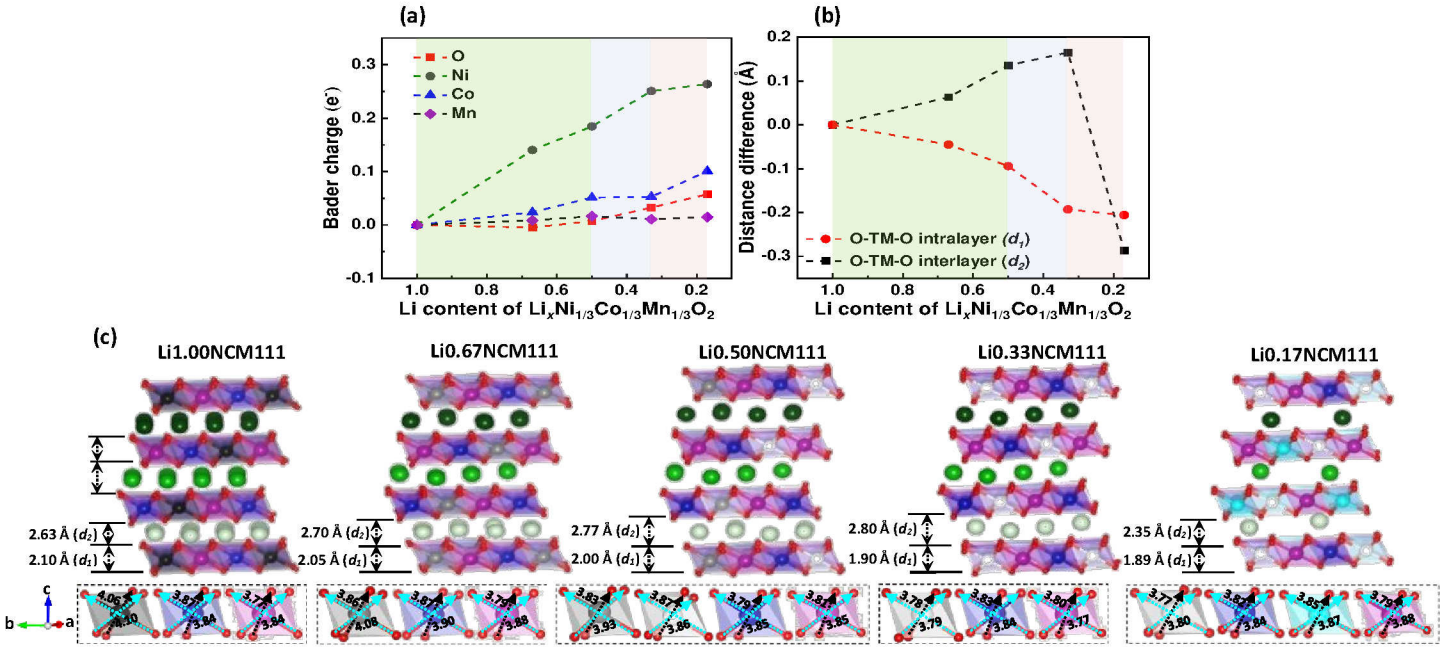

Fig. 4 Calculated (a) Bader Charges and (b) projected intralayer O–TM–O (d_1) and interlayer O–TM–O (d_2) lengths along the *c* axis. (c) Details of bond lengths in TM–O octahedra. Ni, Co, Mn, O, and Li are in grey (dark: $Ni^{(2-\Delta)+}$, light: $Ni^{(3-\Delta)+}$, white: $Ni^{(4-\Delta)+}$, blue (dark: $Co^{(3-\Delta)+}$, light: $Co^{(4-\Delta)+}$, purple, red, and green (lighter at deeper layers), respectively.

Fig. 4a, however, indicate that O anions are only slightly reduced and therefore their charge magnitudes probably play no significant role in controlling the O–O interaction. We therefore propose that the expansion of d_2 is mainly because of vanishing of attractive electrostatic interactions of removed Li ions with O anions. As the expansion of d_2 is larger than the contraction of d_1, the *c* lattice parameter slightly increases. Further removing 0.17 Li from Li0.67NCM111 results in a contraction of d1 by 2.40 %, which is larger than the 2.15 % contraction arising when x = 1.00 → 0.67. This is because, due to the further oxidation, the J–T distortion of half Ni cations in the unit cell is released. In this case, the oxidation of O anions (see Fig. 4a) tends to shrink d_2. However, due to vanishing Li–O interactions, d_2 expands by 3.77 %. Due to the larger expansion of d_2 than the contraction of d_1, the c lattice parameter still increases. However, removing 0.17 Li from Li0.50NCM111 causes d_1 to shrink strongly by 4.93 % which is due to the fact that J–T distortion is lifted in all Ni cations. This contraction is larger than the expansion of 1.05 % in d_2 which is not as large as expected from x = 1.00 → 0.50 as O anions are significantly oxidized. In this case, the impact of disappearing (attractive) electrostatic interaction of removed Li ions with O anions is weaker than that of oxidation of O anions on the O–O separation. The larger contraction of d_1 compared to the expansion of d_2 leads to the shortening of *c* with respect to not only Li0.67NCM111 but also Li1.00NCM111. Although the previous studies proposed that the contraction of *c* is due to the oxidation of O, but we show that this is mainly due to the vanishing of J–T distortion in NiO_6 octahedra. Upon removing 0.17 Li from Li0.33NCM111, d_1 shrinks only slightly by 0.68 % and not as large as from x = 0.50 to x = 0.33. This is because that all Ni cations have been already oxidized to (4–Δ)+ at x = 0.33, and now half Co cations are oxidized to (4–Δ)+ at x = 0.17.

The radius change of a Co cation upon oxidation from (3–Δ)+ to (4–Δ)+ was estimated by other groups to be only from 0.545 Å to 0.53 Å, which is much smaller than that of a Ni cation upon a similar oxidation (0.56 Å to 0.48 Å). [45–48] Therefore, contraction of d_1 is small. On the other hand, d_2 also shrinks significantly for x = 0.33 → 0.17. This is because most of attractive electrostatic Li–O interactions are absent for x = 0.17 letting O–TM–O layers to slide with respect to each other. Figure 5 shows that the first and second O-TM-O layers (counted from the topmost layer) move in-plane direction so that their TM ions become closer to the bottom of the TMS of the third O-TM-O layer. The sliding of first layer is almost two times larger than

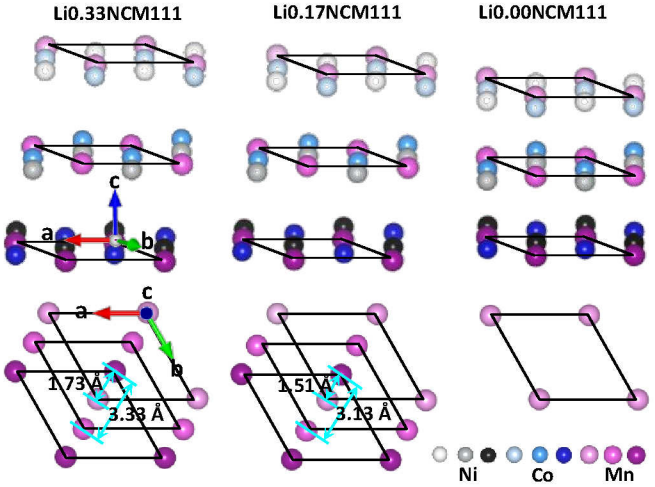

Fig. 5 Side views of TM layers and top views of Mn layers in O3 phase of Li0.33NCM111 and Li0.17NCM111 as well as O1 phase of Li0.00NCM111. In-plane distances between arbitrary Mn ions of different layers are shown in the bottom.

that of second layer. Moreover, O anions have less negative charge (see Fig. 4a) leading to a weaker repulsive O–O interaction. Thus, the *c* lattice parameter decreases dramatically.

To explain the changes in *a* with delithiation we used the average TM–O bond lengths in Fig. 4 to determine creation or suppression of J–T distortions in TM–O octahedra. When x = 1.00 → 0.67, *a* decreases from 2.88 Å to 2.86 Å which is due to the oxidation of all Ni cations from (2−Δ)+ to (3−Δ)+. Upon the oxidation, $Ni^{(3-\Delta)+}$–O octahedra undergo Jahn–Teller (J–T) distortions in which the length of a shrinks from 4.06 Å to 3.86 Å. However, no J–T distortion occurs for $Co^{(3-\Delta)+}$–O and $Mn^{(4-\Delta)+}$–O octahedra since there is no significant change in the oxidation states of Co and Mn. The projection of contraction of equatorial Ni–O bonds on the axis *a* leads to the decrease in the value *a*. The reason of further contraction of a from x = 0.67 (*a* = 2.86 Å) to x = 0.33 (*a* = 2.84 Å) in Fig. 2 is the vanishing of J–T distortion in $Ni^{(4-\Delta)+}$–O leading to similar values of equatorial and axial Ni–O bond lengths. The reason of increase in a for x = 0.33 (*a* = 2.84 Å) → x = 0.17 (*a* = 2.86 Å) in Fig. 2 is because that i) ionic radius of $Co^{(4-\Delta)+}$ in the latter case does not change much with respect to $Co^{(3-\Delta)+}$ in the former case,[47] while ii) the in-plane electrostatic repulsion between $Co^{(4-\Delta)+}$ cations with each other and other cations enhances.

To check the possibility of phase transition from O3 to O1 through a deep delithiation, we modelled Li0.17NCM111 and Li0.00NCM111 in O1 phases (see Fig. S5 in SI). Our DFT-SCAN calculation shows that O3 phase is more favorable than O1 for x = 0.17, which is in spite of a slight sliding of the O–TM–O layer-stacking in Li0.17NCM111 (Fig. 5). However, the O1 phase becomes more favorable than the O3 one for the fully-delithiated case. This finding agrees with the experimental observations by Choi *et al.*[23] and Yin *et al.*[48] showing a O3 → O1 phase transition for deep delithiation levels. Furthermore, we computed the total Coulomb energies for the DFT-SCAN calculated structures of O1 and O3 phases using Bader charges. It is found that the latter structure is electrostatically more favorable for x = 0.17, while the former is more favorable for x = 0.00. The total Coulomb energy for Li0.00NCM111 is, however, calculated to be lower in O3 than O1 phase when considering formal charge states of 4+ for TMs and 2- for O ions. Since the Bader charges on ions are larger in the O1 phase than the other phase of Li0.00NCM111 (Tab. S2 in SI), the O3→O1 phase transition is expected to be driven by the strengthening of ionic bonds and electrostatic interactions.

Conclusions

Here, we showed a computational approach to simulate and understand the variation of lattice sizes of layered cathode materials with delithiation/lithiation. It was found that an extensive Coulomb energy analysis and DFT calculations is required to find arrangement of Li ions in these materials at different level of charge/discharge. Among PBE, PBE+U, and SCAN functional, the last one can compute lattice parameters (*a*, *b*, and *c*) of $Li_xNi_{1/3}Co_{1/3}Mn_{1/3}O_2$ (Li*x*NCM111) as function of Li concentration in better agreement with experimental data. A detailed analysis of local spin polarization, spin density difference plot, density of states, and Bader charges was then applied to gain insight into the nature of delithiation-induced oxidation and lattice size change in this system. Delithiation of Li*x*NCM111 from x = 1.00 to 0.67 leads to the $Ni^{(2-\Delta)+}$ → $Ni^{(3-\Delta)+}$ oxidation of all Ni cations. Although this causes the intralayer O–TM–O length along *c* (d_1) to become slightly shorter, but this contraction is smaller than the expansion of interlayer O–TM–O length along *c* (d_2) leading to the increase in the c parameter. The expansion is due to the vanishing of attractive electrostatic Li–O interaction. Although equatorial Ni–O bonds shrink significantly, the axial ones remain almost unchanged due to the J–T distortion. For this reason, the parameter a, which is influenced by the projection of equatorial $Ni^{(3-\Delta)+}$–O bond length on this axis, undergoes a small contraction. From x = 0.67 to 0.50, the value of c increases slightly due to a further vanishing of attractive electrostatic Li–O interaction. This is in spite of suppression of J–T distortion in half of Ni cations which results in the contraction of intralayer O–TM–O bonds along the *c* and *a* direction. Therefore, the length of a which is controlled by the in-plane projection of O–TM–O bonds is shortened. From x = 0.50 to 0.33, all Ni cations undergo a $Ni^{(3-\Delta)+}$ → $Ni^{(4-\Delta)+}$ oxidation. In this case, the J–T distortion in all NiO_6 octahedra is relieved leading to a large contraction of d_1. For this reason, the size of a decreases further. Although the value of d_2 increases due to further vanishing of attractive electrostatic Li–O interaction, but this expansion is not large enough because of the decrease in the negative charge (i.e. oxidation) of O anions. Therefore, the small expansion of d_2 cannot overcome the large shrinkage of d1. For this reason, the value of c contracts. Finally, from x = 0.33 to x = 0.17, $Co^{(3-\Delta)+}$ → $Co^{(4-\Delta)+}$ oxidation of several cations occurs. Since the radius of oxidized Co cations does not reduce much, the increase in the electrostatic repulsion between $Co^{(4-\Delta)+}$ with other cations lead to an increase in a. However, the c value shrinks significantly, which is due to the in-plane displacements of O–TM–O layers with respect to each other to pack in the direction *c*. At higher concentrations of Li, the sliding of O–TM–O layers does not take place because Li ions keep O–TM–O layers together. Furthermore, our calculations show that for x = 0.00 at which O anions are oxidized more strongly than higher Li concentration cases a phase transition from O3 to O1 occurs in the absence of Li ions that act as glue between O–TM–O layers. Our total Coulomb energy calculation indicates that the O3 → O1 phase transition is driven by increased strength of ionic bonds and electrostatic interaction. A comparison between PBE, PBE+*U*, and SCAN functional results demonstrates that the last one is generally the best choice to predict the lattice parameters as well as magnetic properties. However, all three functionals can qualitatively predict the lattice parameters and volume change correctly.

Theoretical methods

Spin-polarized DFT calculations were carried out using the projector-augmented plane-wave (PAW)[40] pseudopotential which was implemented in the Vienna *Ab Initio* Simulation Package (VASP).[41] To

examine the effect of XC functional on the results, PBE, PBE+*U*, and SCAN were used. The *U–J* (hereafter called *U*) values for Ni, Co, and Mn are 6.8 eV, 5.9 eV, and 5.2 eV respectively. We also further check the influence of *U* value on lattice parameter and volume by considering *U* values of 5 eV and 8 eV for Ni. We only studied the different *U* values for Ni because Ni is the active cation for a wide range of lithium concentrations of 1.00 > *x* > 0.33. To model bulk $Li_xNi_{1/3}Co_{1/3}Mn_{1/3}O_2$ (LixNCM111) a structure with a space group of $R\bar{3}m$ and unit cell of [√3 × √3]R30-type symmetry (1×1×1 unit cell: $Li_9Ni_3Co_3Mn_3O_{18}$) was applied. A 1×1×1 unit cell was considered to calculate total Coulomb energies for *x* = 0.67 and *x* = 0.33, while a 2×2×1 supercell ($Li_{36}Ni_{12}Co_{12}Mn_{12}O_{72}$) was used to calculate total Coulomb energies for *x* = 0.50 and *x* = 0.17 as well as all DFT calculations for 1.00 ≥ *x* ≥ 0.00. A Gamma-centered *k*- point mesh of 2×2×1 and an energy cut off of 500 eV were applied for the 2×2×1 supercell. An electronic and force convergence criterion of 10^{-4} eV and 10^{-3} eV/Å, respectively, were considered. Total Coulomb energy calculations were carried out using the so-called supercell code.[42] Atomic structures were visualized with the VESTA program.[43]

Author contributions

L.-Y. K. has performed the calculations. L. -Y. K, O. G., and P. K. analysed the data.

Conflicts of interest

The authors declare no competing interests.

Acknowledgements

Authors gratefully acknowledge support from the "Bundesministerium für Bildung und Forschung" (BMBF) as well as the computing time granted through JARA-HPC on the supercomputer JURECA at Forschungszentrum Jülich.

Notes and references

1 J.-M. Tarascon and M. Armand, *Nature*, 2001, **414**, 359−367.
2 M. Winter, B. Barnett and K. Xu, *Chem. Rev.*, 2018, **118,** 11433−11456.
3 N. Nitta, F. Wu, J. T. Lee and G. Yushin, *Mater. Today*, 2015, **18,** 252−264.
4 A. Yano, M. Shikano, A. Ueda, H. Sakaebe and Z. Ogumi, *J. Electrochem. Soc.*, 2017, **164**, A6116−A6122.
5 C. S. Yoon, D.-W. Jun, S.-T. Myung and Y.-K Sun, *ACS Energy Lett.*, 2017, **2**, 1150−1155.
6 T. Ohzuku, A. Ueda and M. Nagayama, *J. Electrochem. Soc.*, 1993, **140**, 1862−1870.
7 A. Rougier, P. Gravereau and C. Delmas, *J. Electrochem. Soc.*, 1996, **143**, 1168−1175.
8 T. Uyama, K. Mukai and I. Yamada, *RSC Adv.*, 2018, **8**, 26325−26334.
9 M. S. Whittingham, *Chem. Rev.*, 2004, **104**, 4271−4302.
10 P. G. Bruce, A. R. Armstrong and R. L. Gitzendanner, *J. Mater. Chem.*, 1999, **9**, 193−198.
11 O. Tsutomu, and M. Yoshinari, *Chem. Lett.*, 2001, **30**, 642−643.
12 A. M. Dreizler, N. Bohn, H. Geßwein, M. Müller, J. R. Binder, N. Wagner and K. A. Friedrich, *J. Electrochem. Soc.*, 2018, **165**, A273−A282.
13 W. Hua, Z. Wu, M. Chen, M. Knapp, X. Guo, S. Indris, J. R. Binder, N. N. Bramnik, B. Zhong, H. Guo, S. Chou, Y.-M. Kang and H. Ehrenberg, *J. Mater. Chem. A*, 2017, **5**, 25391−25400.
14 G.-L. Xu, Q. Liu, K. K. S. Lau, Y. Liu, X. Liu, H. Gao, X. Zhou, M. Zhuang, Y. Ren, J. Li, M. Shao, M. Ouyang, F. Pan, Z. Chen, K. Amine and G. Chen, *Nat. Energy*, 2019, **4**, 484−494.
15 K. Min and E. Cho, *Phys. Chem. Chem. Phys.*, 2018, **20**, 9045−9052.
16 A. O. Kondrakov, A. Schmidt, J. Xu, H. Geßwein, R. Mönig, P. Hartmann, H. Sommer, T. Brezesinski and J. Janek, *J. Phys. Chem. C*, 2017, **121**, 3286−3294.
17 J. Kasnatscheew, U. Rodehorst, B. Streipert, S. Wiemers-Meyer, R. Jakelski, R. Wagner, I. C. Laskovic and Martin Winter, *J. Electrochem. Soc.*, 2016, **163**, A2943−A2950.
18 J. C. Garcia, J. Bareño, J. Yan, G. Chen, A. Hauser, J. R. Croy and H. Iddir, *J. Phys. Chem. C*, 2017, **121**, 8290−8299.
19 R. C. Longo, F. Kong, C. Liang, D.-H. Yeon, J. Yoon, J.-H. Park, S.-G. Doo and K. Cho, *J. Phys. Chem. C*, 2016, **120**, 8540−8549.
20 H. Sun and K. Zhao, *J. Phys. Chem. C*, 2017, **121**, 6002−6010.
21 G. Luo, J. Zhao, X. Ked, P. Zhang, H. Sun and B. Wang, *J. Electrochem. Soc.*, 2012, **159**, A1203−A1208.
22 J. Y. Lee, J. Y. Kim, H. I. Cho, C. H. Lee, H. S. Kim, S. U. Lee, T. J. Prosa, D. J. Larson, T. H. Yu and J.-P. Ahn, *J. Power Sources*, 2018, **379**, 160−166.
23 J. Choi and A. Manthiram, *J. Electrochem. Soc.*, 2005, **152**, A1714−A1718.
24 C. F. Petersburg, Z. Li, N. A. Chernova, S. M. Whittingham and F. M. Alamgir, *J. Mater. Chem.*, 2012, **22**, 19993−20000.
25 Z. Li, N. A. Chernova, M. Roppolo, S. Upreti, C. Petersburg, F. M. Alamgir and M. S. Whittingham, *J. Electrochem. Soc.*, 2011, **158**, A516−A522.
26 W. Hua, B. Schwarz, M. Knapp, A. Senyshyn, A. Missiul, X. Mu, S. Wang, C. Kubel, J. R. Binder, S. Indris and H. Ehrenberg, *J. Electrochem. Soc.*, 2019, **166**, A5025−A5032.
27 L. de Biasi, B. Schwarz, T. Brezesinski, P. Hartmann, J. Janek and H. Ehrenberg, *Adv. Mater.*, 2019, **31**, 1900985.
28 A. O. Kondrakov, H. Geßwein, K. Galdina, L. de Biasi, V. Meded, E. O. Filatova, G. Schumacher, W. Wenzel, P. Hartmann, T. Brezesinski and J. Janek, *J. Phys. Chem. C*, 2017, **44**, 24381−24388.
29 B. J. Hwang, Y. W. Tsai, D. Carlier and G. Ceder, *Chem. Mater.*, 2003, **15**, 3676−3682.
30 Y. Koyama, N. Yabuuchi, I. Tanaka, H. Adachi and T. Ohzuku, *J. Electrochem. Soc.*, 2004, **151**, A1545−A1551.
31 J. P. Perdew, K. Burke and M. Ernzerhof, *Phys. Rev. Lett.*, 1996, **77**, 3865−3868.
32 K. Min, K. Kim, C. Jung, S.-W. Seo, Y. Y. Song, H. S. Lee, J. Shin and E. Cho, *J. Power Sources*, 2016, **315**, 111−119.
33 J. Hubbard, *Phys. Eng. Sci.*, 1963, **276**, 238−257.
34 J. Heyd, G. E. Scuseria and M. Ernzerhof, *J. Chem. Phys.*, 2003, **118**, 8207−8215.
35 J. W. Sun, A. Ruzsinszky and J. P. Perdew, *Phys. Rev. Lett.*, 2015, **115**, 036402.
36 J. Sun, R. C. Remsing, Y. Zhang, Z. Sun, A. Ruzsinszky, H. Peng, Z. Yang, A. Paul, U. Waghmare, X. Wu, M. L. Klein and J. P. Perdew, *Nat. Chem.*, 2016, **8**, 831−836.
37 J. P. Perdew, J. Sun, R. M. Martin and B. Delley, *Int. J. Quantum Chem.*, 2016, **116**, 847−851.
38 Y. Zhang, D. A. Kitchaev, J. Yang, T. Chen, S. T. Dacek, R. A. Sarmiento-Pérez, M. A. L. Marques, H. Peng, G. Ceder, J. P. Perdew and J. Sun, *npj Comput. Mater.*, 2018, **4,** 9.
39 A. Chakraborty, M. Dixit, D. Aurbach and D. T. Major, *npj Comput. Mater.*, 2018, **4**, 60.

40 P. E. Blöchl, *Phys. Rev. B: Condens. Matter Mater. Phys.*, 1994, **50**, 17953–17979.
41 G. Kresse and J. Furthmüller, *Phys. Rev. B: Condens. Matter Mater. Phys.*, 1996, **54**, 11169–11186.
42 K. Okhotnikov, T. Charpentier and S. Cadars, *J. Cheminformatics*, 2016, **8**.
43 K. Momma and F. Izumi, *J. Appl. Crystallogr.*, 2011, **44**, 1272–1276.
44 K. Hoang and M. Johannes, *Chem. Mater.*, 2016, **28**, 1325–1334.
45 H. H. Li, *Chem. Mater.*, 2007, **19**, 2551–2565.
46 K.-S. Lee, S.-T. Myung, K. Amine, H. Yashiro and Y.-K. Sun, *J. Electrochem. Soc.*, 2007, **154**, A971–A977.
47 R. D. Shannon, *Acta Crystallogr A.*, 1976, **32**, 751–767.
48 S.-C. Yin, Y.-H. Rho, I. Swainson and L. F. Nazar, *Chem. Mater.*, 2006, **18**, 1901– 1910.
49 Y. Idemoto, T. Mochizuki, K. Ui and N. Koura, *J. Electrochem. Soc.*, 2006, **153,** A418-A424.
50 M. Dixit, B. Markovsky, F. Schipper, D. Aurbach and D. T. Major, *J. Phys. Chem. C*, 2017, **121,** 22628–22636.
51 M. D. Radin, S. Hy, M. Sina, C. Fang, H. Liu, J. Vinckeviciute, M. Zhang, M. S. Whittingham, Y. S. Meng and A. Van der Ven, *Adv. Energy Mater.*, 2017, **7,** 1602888.
52 M. E. Arroyo y de Dompablo, C. Marianetti, A. Van der Ven and G. Ceder, *Phys. Rev. B*, 2001, **63,** 144107.
53 H. Chen, C. L. Freeman and J. H. Harding, *Phys. Rev. B*, 2011, **84,** 085108.
54 S. Zhang, J. Ma, Z. Hu, G. Cui and L. Chen, *Chem. Mater.*, 2019, **31,** 6033−6065.
55 Y. W. Tsai, B. J. Hwang, G. Ceder, H. S. Sheu, D. G. Liu and J. F. Lee, *Chem. Mater.*, 2005, **17,** 3191−3199.
56 D.-H. Seo, A. Urban and G. Ceder, *Phys. Rev. B*, 2015, **92,** 115118.
57 I. Buchberger, S. Seidlmayer, A. Pokharel, M. Piana, J. Hattendorff, P. Kudejova, R. Gilles and H. A. Gasteiger, *J. Electrochem. Soc.*, 2015, **162,** A2737−A2746.
58 L. de Biasi, A. O. Kondrakov, H. Geßwein, T. Brezesinski, P. Hartmann and J. Janek, *J. Phys. Chem. C*, 2017, **121,** 26163−26171.
59 W.-S. Yoon, M. Balasubramanian, K. Y. Chung, X.-Q. Yang, J. McBreen, C. P. Grey and D. A. Fischer, *J. AM. CHEM. SOC.*, 2005, **127,** 17479−17487.
60 T. Ohnum and T. Kobayashi, RSC Adv., 2019, **9,** 35655.
61 M. Dixit, M. Kosa, O. S. Lavi, B. Markovsky, D. Aurbach and D. T. Major, *Phys. Chem. Chem. Phys.*, 2016, **18,** 6799−6812.
62 I. Saadoune, M. Ménétrier and C. Delmas, *J. Mater. Chem.*, 1997, **7,** 2505–2511.